A bacterial cytolinker couples positioning of magnetic organelles to cell shape control

Daniel Pfeiffer[a,1], Mauricio Toro-Nahuelpan[a,b,2], Ram Prasad Awal[a], Frank-Dietrich Müller[a], Marc Bramkamp[c], Jürgen M. Plitzko[b], and Dirk Schüler[a]

[a]Department of Microbiology, University Bayreuth, 95447 Bayreuth, Germany; [b]Department of Molecular Structural Biology, Max Planck Institute of Biochemistry, 82152 Planegg-Martinsried, Germany; and [c]Institute for General Microbiology, Christian-Albrechts-University, 24118 Kiel, Germany

Magnetotactic bacteria maneuver within the geomagnetic field by means of intracellular magnetic organelles, magnetosomes, which are aligned into a chain and positioned at midcell by a dedicated magnetosome-specific cytoskeleton, the "magnetoskeleton." However, how magnetosome chain organization and resulting magnetotaxis is linked to cell shape has remained elusive. Here, we describe the cytoskeletal determinant CcfM (curvature-inducing coiled-coil filament interacting with the magnetoskeleton), which links the magnetoskeleton to cell morphology regulation in *Magnetospirillum gryphiswaldense*. Membrane-anchored CcfM localizes in a filamentous pattern along regions of inner positive-cell curvature by its coiled-coil motifs, and independent of the magnetoskeleton. CcfM overexpression causes additional circumferential localization patterns, associated with a dramatic increase in cell curvature, and magnetosome chain mislocalization or complete chain disruption. In contrast, deletion of *ccfM* results in decreased cell curvature, impaired cell division, and predominant formation of shorter, doubled chains of magnetosomes. Pleiotropic effects of CcfM on magnetosome chain organization and cell morphology are supported by the finding that CcfM interacts with the magnetoskeleton-related MamY and the actin-like MamK via distinct motifs, and with the cell shape-related cytoskeleton via MreB. We further demonstrate that CcfM promotes motility and magnetic alignment in structured environments, and thus likely confers a selective advantage in natural habitats of magnetotactic bacteria, such as aquatic sediments. Overall, we unravel the function of a prokaryotic cytoskeletal constituent that is widespread in magnetic and nonmagnetic spirilla-shaped Alphaproteobacteria.

magnetotaxis | magnetosome | cytoskeleton | MamK | MreB

It has become evident that prokaryotes are sophisticated organisms with a high level of intracellular organization, which exhibit complex organelles and cytoskeletal networks. One of the most intriguing examples is found in magnetotactic bacteria (MTB), which present an intricate cytoskeleton that controls the organization of magnetic organelles, the magnetosomes. These membrane-enveloped crystals of a magnetic iron mineral serve for navigation within the geomagnetic field (magnetotaxis) toward preferred micro- or anoxic environments (1). To ensure alignment of MTB in the geomagnetic field, magnetosomes are arranged in chains, and formation of the magnetosome chain, as well as its repositioning and equipartitioning during the cell cycle, must be precisely controlled. In the magnetotactic Alphaproteobacterium *Magnetospirillum gryphiswaldense* and related MTB, concatenation of individual magnetosomes into a coherent and single linear chain is governed by the actin-like MamK, which forms cell-spanning filaments and acts as a scaffold for dynamic magnetosome chain assembly (2, 3). Treadmilling of MamK filaments causes the repositioning of magnetosome chains at midcell upon cell division (4, 5). Magnetosomes are connected to MamK by the acidic MamJ protein (6, 7). Recently, the membrane-bound MamY protein was reported as an additional essential topological landmark for magnetosome chain localization. In *M. gryphiswaldense*, MamY ensures positioning of magnetosome chains at regions of highest inner positive-cell curvature (i.e., the geodetic

axis), thus aligning the magnetosome chain to the motility axis within a helical cell (8).

Recent observations indicate that all determinants for magnetosome chain formation and positioning [MamJ, MamK, and MamY; altogether the "magnetoskeleton" (8)] are in fact required for efficient navigation within the geomagnetic field (9). Magnetotaxis was further shown to enhance navigation through porous media (10), resembling the compact and dense natural habitats of MTB, such as muddy aquatic sediments. In non-MTB, a curved cell shape is important for efficient motility in related structured and highly viscous environments (11–14) by facilitating the migration through such gel-like media (15). While the sophisticated system for magnetosome chain positioning in MTB suggests that magnetotaxis is linked to cell shape, it is entirely unknown whether the magnetoskeleton is functionally connected to the general cytoskeleton-controlling cell shape in MTB. Shape-determining cytoskeletal proteins usually function by organizing the location and activity of periplasmic cell wall synthesis enzymes (16). A key player of the bacterial cytoskeleton is MreB that, like MamK, belongs to the actin superfamily of cytoskeletal protofilaments (17) and is found in most walled bacteria with elongated cell shape (16, 17). MreB orients circumferentially in short filaments along greatest negative principal membrane curvature and orchestrates centers of cell wall synthesis to maintain elongated cell shape (18). In addition to

Significance

The bacterial cytoskeleton is an intricate meshwork of filaments, fundamental for cell shape determination and subcellular organization. An elaborate example is found in magnetotactic bacteria, which employ a distinct cytoskeleton, the "magnetoskeleton," to align magnetic nanoparticles (magnetosomes) for navigation within the geomagnetic field. Thus far, cytoskeletal determinants for cell shape in magnetotactic bacteria, and whether those are functionally linked to the magnetoskeleton, has remained unknown. Here, we describe the structural protein CcfM (curvature-inducing coiled-coil filament interacting with the magnetoskeleton), which functions as an interconnector (cytolinker) between the magnetoskeleton and cytoskeleton. CcfM not only controls cell curvature, but also formation of coherent cell-spanning magnetosome chains, enhancing magnetic navigation within environmental habitats.

Fig. 1. CcfM localizes in filamentous patterns and affects cell curvature and magnetosome chain positioning. (*A*) CcfM domain structure. CC, putative coiled-coil motifs (black = high confidence; gray = medium to low confidence); TM, putative transmembrane segments; numbers indicate amino acid positions. (*B*) Representative 3D-SIM micrographs of cells expressing GFP-CcfM from its native chromosomal locus and promoter (*i*, strain *ccfM::gfp-ccfM*) and after random chromosomal insertion of a Tn5-P$_{tet}$–based expression cassette in the wild-type background (*ii*, 5 h and *iii–iv*, 25 h postinduction). For each subfigure: *Left* column, maximum-intensity projection (brightfield image as *Inset*); *Right* column, top-left to bottom-right corner: consecutive *z*-slices with a distant spacing of 150 nm (*i* and *ii*) and 200 nm (*iii* and *iv*), respectively. Calibration bars denote the intensity of fluorescence. (Scale bars, 1 μm.) (*C*) DIC (*Upper*) and maximum-intensity projection of deconvolved *z*-stack (*Lower*) of elongated Δ*popZ* cells expressing GFP-CcfM from Tn5-P$_{tet}$ (*i*, 7 h; *ii*, 24 h postinduction). (Scale bars, 3 μm.) (*D*) 3D-SIM maximum-intensity projections (brightfield as *Inset*) of mNeonGreen-CcfM expressed from Tn5-P$_{tet}$ in the wild-type (*i*) and Δ*ccfM* (*ii*) background (5 h postinduction). Calibration bars indicate the intensity of fluorescence. (Scale bars, 1 μm.) (*E*) TEM micrographs of overly curved CcfM-overexpressing cells (wild-type + Tn5-P$_{tet}$-*ccfM*, 24 h postinduction). Magnetosomes and flagella are marked by white and black arrowheads, respectively. (Scale bars, 1 μm.) (*F*) CET of a CcfM-overproducing cell in the absence of MamK and MamY (Δ*mamKY* + Tn5-P$_{tet}$-*ccfM*, 24 h postinduction). (*i*) Individual 5.24-nm-thick tomographic slices with different *z*-depth through the tomogram depicting the curved cell and the putative CcfM-related structure (purple arrowheads) close to the inner membrane. The localization of the sheet-like structure correlates with the positioning of CcfM observed by 3D-SIM. IM/OM, inner/outer membrane; PG, peptidoglycan layer. (Scale bars, 100 nm.) (*ii* and *iii*) Three-dimensional rendering of the tomographed cell. Inner/outer membranes and the peptidoglycan layer are depicted in blue, vesicles are yellow. The putative CcfM structure is purple. (*iv*) Membranogram depicts a projection of the tomogram at a certain distance from the membrane. The putative CcfM structure is indicated by purple arrowheads. Thickness of the rendered shell is 2.1 nm; distance from the membrane is 14.7 nm.

MreB, which exhibits dynamics, cell shape-determining properties have also been attributed to bacterial cytoskeletal elements that assemble in a nucleotide-independent manner, commonly acting as a rather static scaffold (17, 19). Such proteins are often characterized by the presence of the coiled-coil structural motif, which is formed through the parallel or antiparallel association of α-helices coiled together like the strands of a rope (17). In the Alphaproteobacterium *Caulobacter crescentus*, the coiled-coil protein crescentin (CreS) forms a filamentous structure required to maintain curved cell shape and has been described as an intermediate-filament equivalent (20–22). Further coiled-coil filament-forming proteins, some of which also interact or function concomitantly with cell wall biosynthetic enzymes and MreB, have been, for example, described in the pathogenic spirilla-shaped Epsilonproteobacterium *Helicobacter pylori* (13, 23–27), the spirochete *Leptospira biflexa* (28, 29), the predatory Deltaproteoacterium *Bdellovibrio bacteriovorus* (30), or the curved rod Gammaproteobacterium and pathogen *Vibrio cholerae* (11).

Here, we report the structural determinant CcfM (curvature-inducing coiled-coil filament interacting with the magnetoskeleton)

MICROBIOLOGY

in *M. gryphiswaldense*. Using reverse genetics and fluorescence microscopy, we show that CcfM localizes in filamentous patterns along regions of inner positive-cell curvature by its coiled-coil motifs, and independent of magnetosome-specific genes, indicating that formation of a filamentous structure is an inherent feature of CcfM. We provide evidence that CcfM is an interactor of the magnetosome chain assembly proteins MamK and MamY, and that CcfM promotes formation of single chains of magnetosomes that extend into subpolar-to-polar intracellular regions, in agreement with its native localization. Moreover, we demonstrate that CcfM affects cell curvature and division, and interacts with the key cytoskeletal determinant MreB, suggesting that CcfM functions as an interconnecting element (cytolinker) between the magnetoskeleton and the general cytoskeleton. Altered cell morphology and magnetosome chain organization upon deletion of *ccfM* causes impaired motility and magnetic alignment in complex structured environments, substantiating its role as a mediator between cell shape and magnetosome chain organization.

Results

CcfM Is a Putative Coiled-Coil Protein. During a candidate search for motility determinants in *M. gryphiswaldense*, we identified CcfM (MSR1_16830, genome accession no. CP027526) (*SI Appendix,* Fig. S1*A*), employing the Kyoto Encyclopedia of Genes and Genomes (KEGG) database ortholog search and TipN protein as a query, which controls division site placement and polar flagellation in *C. crescentus* (31, 32). CcfM (predicted molecular mass = 105.5 kDa) exhibits similar subdomain architecture as TipN: That is, two N-terminal transmembrane-spanning segments and a large cytoplasmic coiled-coil–rich region (Fig. 1*A* and *SI Appendix,* Fig. S1*B*). In contrast, CcfM displays only low amino acid sequence identity (~20%) to TipN or other related coiled-coil proteins (*SI Appendix,* Table S1); hence, CcfM is rather unlikely to be a TipN ortholog. However, CcfM orthologs (E-value threshold of 10^{-5}) (*SI Appendix, Supplemental Materials and Methods*) are present, mainly in bacteria of the order Rhodospirillales with helical or vibrioid cell shape, including both magnetic and nonmagnetic members (*SI Appendix,* Fig. S2). National Center for Biotechnology Information conserved domains and KEGG motif searches using CcfM as a query revealed bacterial proteins containing coiled-coil motifs, such as "structural maintenance of chromosomes proteins" (E-value ≥ 1.26×10^{-4}) and "methyl-accepting chemotaxis proteins" (E-value ≥ 1.72×10^{-3}), but also motifs related to Apolipophorin-III (ApoLp-III) and Apolipoprotein A1/A4/E (E-value ≥ 3.02×10^{-3}) within the coiled-coil–rich C-terminal part of CcfM (*SI Appendix,* Fig. S1*B*). Apolipophorins and related Apolipoproteins are characterized by structurally flexible bundles of amphipathic α-helices that undergo conformational changes (*SI Appendix,* Fig. S1*C*) to mediate lipid interactions in eukarya (33–35), but related domains are also found in other large bacterial coiled-coil proteins (*SI Appendix,* Table S1) (36, 37).

CcfM Localizes in Filamentous Patterns along Regions of Positive Inner Cell Curvature. To investigate CcfM localization, we constructed various N- and C-terminal fluorescent fusions (*SI Appendix*). By three-dimensional (3D) structured illumination microscopy (3D-SIM) (Fig. 1*B* and *SI Appendix,* Fig. S3*A*) and conventional epifluorescence microscopy (*SI Appendix,* Fig. S3*C*), we observed that GFP-CcfM localized in a filamentous pattern along the positive inner curvature of the cell (i.e., forming a line traversing the shortest distance from pole to pole), thereby touching the regions of the cell envelope that are bent inward toward the cytoplasm [i.e., the minor cell axis (14) or geodetic axis (8)]. Expression of GFP-CcfM from its native promoter and chromosomal locus (Fig. 1 *B, i* and *SI Appendix,* Fig. S3 *C, i*) or from an inducible promoter in a Δ*ccfM* strain (*SI Appendix,* Fig. S3 *C, ii*) resulted in a filamentous structure, which appeared less continuous around midcell but exhibited

stronger fluorescence in polar-to-subpolar regions. In contrast, inducible expression in the wild-type background, with native untagged CcfM also present (i.e., overall CcfM levels above the wild-type), caused localization in an almost continuous filamentous pattern (Fig. 1 *B, ii, SI Appendix,* Fig. S3 *A, i* and ii and *C,* iii, and Movie S1). Upon inducible expression, GFP-CcfM was also observed at the cytoplasmic membrane, framing the cell by a weak fluorescence (Fig. 1 *B, ii*).

In addition to filamentous GFP-CcfM structures located at regions of highest inner positive-cell curvature, we observed spiral- or ring-shaped patterns oriented perpendicular to the long cell axis after prolonged induction times, and occasionally longitudinal filamentous structures located at opposing regions of inner negative-cell curvature [i.e., the major cell axis (14)] (Fig. 1 *B, iii* and *iv, SI Appendix,* Fig. S3 *A,* iii and iv and *C,* iv, and Movies S2 and S3). In a Δ*popZ* background, which forms highly elongated cells due to absence of the polar organizer PopZ (38), continuous filamentous GFP-CcfM structures extending over up to ~22 μm were consistently formed (Fig. 1 *C, i*), suggesting that they assemble independently of PopZ, and that their final length is determined by cell length. Overall similar localization patterns were observed with fluorescent fusions of CcfM to the monomeric fluorescent proteins mNeonGreen (39) (mNG-CcfM) (Fig. 1*D* and *SI Appendix,* Fig. S3*B*) or mTurquoise2 (40) (mTurq2-CcfM) (*SI Appendix,* Fig. S3*D*), confirming that filamentous localization of the GFP-CcfM fusion was not an artifact caused by the GFP-tag.

Overproduction of CcfM Promotes Cell Curvature and Interferes with Magnetosome Chain Alignment. Remarkably, inducible overexpression of GFP-CcfM in the wild-type background (Fig. 1 *B, iii* and *iv* and *SI Appendix,* Fig. S3 *A,* iii and iv and *C,* iv) caused formation of highly curved and arc-shaped cells, as well as partially elongated and overly twisted cells, indicating that CcfM influences cell curvature and division. Similar effects on cell curvature were observed upon prolonged expression of GFP-CcfM in the Δ*popZ* strain (Fig. 1 *C, ii*), or by transmission electron microscopy (TEM) upon tag-free overproduction of CcfM (Fig. 1*E*), ruling out that cell morphology changes are caused by the GFP-tag. Quantitative two-dimensional (2D) analysis of cell curvature and 3D-SIM live-cell imaging confirmed that increased cell curvature is driven by CcfM overproduction (*SI Appendix, Supplemental Results* and Figs. S4 and S5 and Movie S4). Filamentous localization and cell curvature-promoting functions of CcfM were independent of the magnetoskeleton and other magnetosome-related proteins (*SI Appendix,* Fig. S6). Cryo-electron tomography (CET) of cells overproducing CcfM in the absence of the filamentous magnetoskeleton-related proteins MamK and MamY revealed a sheet-like structure possibly related to CcfM located 17 ± 1.7 nm (mean ± SD; n = 5 cells) underneath along the geodetic axis of the cellular membrane (Fig. 1*F, SI Appendix,* Fig. S7, and Movies S5 and S6). CcfM truncation studies further suggested that the membrane anchor and some, but not all coiled-coil motifs, are required for robust filamentous CcfM localization, and sufficient to promote cell curvature when expressed in addition to untagged full-length CcfM (*SI Appendix, Supplemental Results* and Fig. S8). Remarkably, TEM also revealed frequent cases of magnetosome chain misplacement (at the major cell axis), or even entire disruption of chains and dispersed magnetosomes in CcfM overproducing cells (Fig. 1*E* and *SI Appendix,* Fig. S9*A*), providing a hint that elevated CcfM levels may interfere with magnetosome chain formation and alignment. These results prompted us to interrogate effects of *ccfM* deletion on cell morphology and magnetosome chain formation and positioning.

***ccfM* Deletion Results in Morphological Defects and Formation of Shorter and Doubled Magnetosome Chains.** Upon *ccfM* deletion, at first glance, Δ*ccfM* cells appeared slightly elongated in comparison
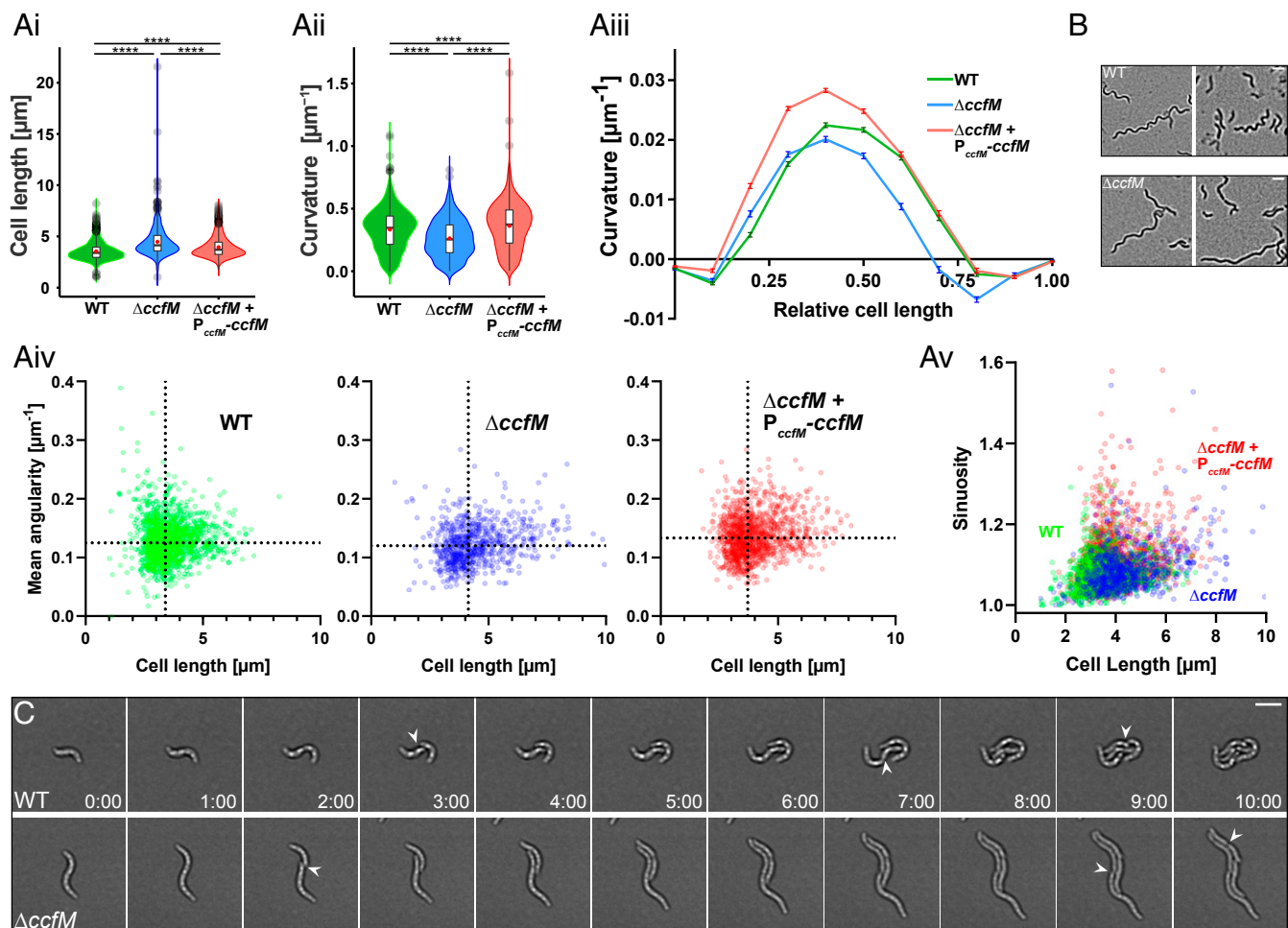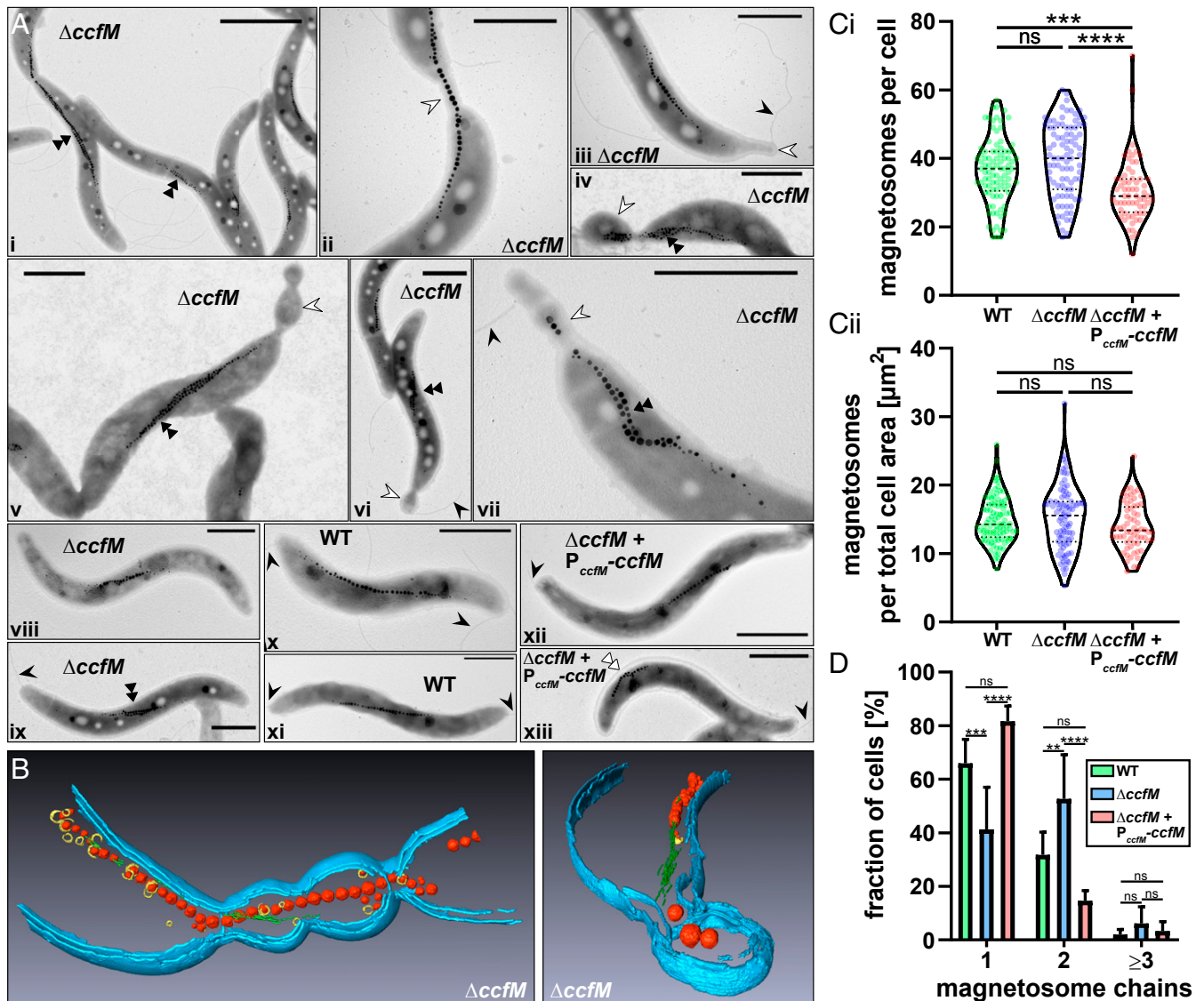
Fig. 2. Deletion of *ccfM* results in altered cell morphology. (*A*) The wild-type (WT) strain, the Δ*ccfM* strain, and the Δ*ccfM* strain complemented *in trans* using a Tn7-based construct (comprising *ccfM* and its putative promoter region; Δ*ccfM* + P$_{ccfM}$-*ccfM*) were analyzed for their (*i*) centerline cell length, (*ii*) curvature, (*iii*) mean curvature (± SEM) along the centerline relative to the normalized cell length, (*iv*) mean angularity, and (*v*) sinuosity versus cell length. Results in *i* and *ii* are presented as box plots and rotated kernel probability density plots to indicate the distribution of the data. The thick horizontal line indicates the median and the red dot indicates the mean. The box represents the interquartile range and the whiskers are extending to the lowest and highest value within 1.5 times the interquartile range from the hinges, respectively. Outliers are colored gray. *P* values were determined by the Kruskal–Wallis test with Dunn's multiple comparison posttest; ****$P < 0.0001$; ns, not significant ($P \geq 0.05$). In *iv* and *v*, dots represent individual cells (extreme values were clipped to better indicate the distribution of the data). Dotted lines in *iv* indicate the median. Measurements are based on exponential growth phase cultures grown in triplicates per strain under microoxic conditions (2% headspace oxygen) in liquid medium. Total numbers of analyzed cells: $n = 1{,}447$ (wild-type), 788 (Δ*ccfM*), and 1,400 (Δ*ccfM* + P$_{ccfM}$-*ccfM*). (*B*) Representative filamentous wild-type and Δ*ccfM* cells (brightfield micrographs) from agar (1.5% [wt/vol]) plate-grown cultures (8 d of incubation at 2% headspace oxygen). (Scale bars, 3 μm.) (*C*) Time-lapse microscopy (brightfield micrographs) of the wild-type and Δ*ccfM* strain on agarose pads. Cell division events are marked by white arrowheads. Time values (in hours and minutes) given in the wild-type panel are valid for both strains. (Scale bar, 3 μm.)

to wild-type cells, which might be related to an overall reduction in cell helicity. Analysis of cells using 2D-based shape descriptors (*SI Appendix, Supplemental Materials and Methods* and *Fig. S4*) indeed confirmed that Δ*ccfM* cells on average are ~1-μm longer and 5 to 21% less curved than wild-type cells (Fig. 2*A* and *SI Appendix, Supplemental Results*). Prolonged growth of *M. gryphiswaldense* on nutrient-rich agar plates led to the occurrence of subpopulations of filamentous helical cells [as also observed in other Alphaproteobacteria (41)], in addition to many cells with increased width or no obvious changes in morphology (Fig. 2*B*). Such filamentous cells of the Δ*ccfM* strain appeared, in general, less regular and exhibited a wider spacing between helical turns, indicating that Δ*ccfM* cells are impaired to modulate their helicity in response to change of the environment. Altered cellular morphology of Δ*ccfM* cells was further observed by time-lapse microscopy (Fig. 2*C*). Subsequent analysis of live-cell time series

revealed a broader distribution of cell lengths, and an accentuated asymmetry of newborn daughter cells for the Δ*ccfM* strain (*SI Appendix, Fig. S10A*), indicating that division at off-center positions in the Δ*ccfM* strain occurred at a higher frequency than in the wild-type, which has been shown to also exhibit asymmetric division (5, 38). Despite the morphological defects, only subtle differences in growth were observed between the wild-type and Δ*ccfM* strain (*SI Appendix, Fig. S10B*).

Moreover, TEM images showed that 8 to 22% of Δ*ccfM* cells possessed "stalk" or "bubble"-like appendages ($n = 502$ cells, four independent experiments) (Fig. 3 *A, iii–vii*, and *SI Appendix, Fig. S9B*), which were only very rarely observed in form of detached minicells. As also revealed by TEM (Fig. 3 *A, ii*) and CET (Fig. 3*B* and Movies S7 and S8), "appendages" likely were remainders from asymmetric division of tubular extensions of the cell division site. Formation of polar flagella and geodetic

Downloaded at MPIs Martinsried on March 1, 2021

Pfeiffer et al.

PNAS | December 15, 2020 | vol. 117 | no. 50 | 32089

MICROBIOLOGY

Fig. 3. Deletion of *ccfM* causes tubular extensions connecting dividing cells and predominant formation of shorter magnetosome double chains. (*A*) Representative TEM micrographs of the Δ*ccfM* strain (*i–ix*), the wild-type (WT) strain (*x* and *xi*), and the Δ*ccfM* strain harboring the Tn7-based trans-complementation construct (*xii* and *xiii*). Appendages are marked with white arrowheads. Flagella are indicated by black arrowheads. Doubled or multiples of magnetosome chains are indicated by black double arrowheads. In *xiii* the magnetosome chain is shifted toward the major axis of the cell (white double arrowhead). (Scale bars, 1 μm.) (*B*) CET 3D rendering of (*Left*) a tubular structure connecting dividing cells and (*Right*) a bulb-like extension of the cell envelope. Magnetite crystals are marked red, magnetosome membrane vesicles are yellow, and the actin-like MamK filament is green. The cellular envelope inner and outer membranes are depicted in blue. (*C*) Magnetosome numbers (*i*) per cell and (*ii*) per total cell area estimated by TEM. Violin plots depict the frequency distribution of the data. The dashed line depicts the median, and dotted lines depict the quartiles. Dots represent measures of individual cells. The numbers of analyzed cells correspond to $n = 93$ (wild-type), 90 (Δ*ccfM*), and 64 (Δ*ccfM* + P$_{ccfM}$-*ccfM*). *P* values were determined by the Kruskal–Wallis test with Dunn's multiple comparison posttest; ***$P < 0.001$; ****$P < 0.0001$; ns, not significant ($P \geq 0.05$). (*D*) Analysis of magnetosome chain number. A chain was defined as chain-like arrangement of greater than or equal to eight magnetosomes, which were interspaced by not more than ~50 nm from each other. Bars depict average percentages of cells harboring the respective numbers of magnetosome chains. Error bars reflect SD between different TEM datasets, greater than or equal to three different datasets were analyzed per strain. The total numbers of analyzed cells correspond to $n = 267$ (wild-type), 382 (Δ*ccfM*), and 63 (transcomplemented Δ*ccfM* strain). Statistical analysis was performed by two-way analysis of variance with Tukey's multiple comparison posttest; **$P < 0.01$; ***$P < 0.001$; ****$P < 0.0001$; ns, not significant ($P \geq 0.05$).

positioning of magnetosome chains were apparently not affected in the absence of *ccfM*, although we observed cases of magnetosome chain mispartitioning (Fig. 3 *A*, *i* and *iv* and *SI Appendix*, Fig. S9*B*). CET further revealed that most magnetosomes located within tubular extensions or appendages were not connected to the MamK filament (Fig. 3*B*). Quantification of absolute magnetosome numbers per cell (Fig. 3 *C*, *i*), and relative to the cell area (Fig. 3 *C*, *ii*) revealed slightly different distributions, but no significant differences between the wild-type

and Δ*ccfM* strain. Remarkably, Δ*ccfM* populations exhibited a significant higher number of cells (~53%) harboring doubled chains of magnetosomes than the wild-type (~32%), and less cells with single chains (wild-type, ~66%; Δ*ccfM*, ~41%) (Fig. 3*D*). Furthermore, in the Δ*ccfM* strain, magnetosomes at subpolar inward-bend regions of the cell often appeared more loosely spaced and scattered than in the wild-type (Fig. 3 *A*, *viii–xi* and *SI Appendix*, Fig. S9 *B* and *C*). Altogether, these results suggested that, while the wild-type tends to organize

magnetosomes in single chains that are longer [in agreement with earlier observations (3)], the Δ*ccfM* strain predominantly forms shorter and doubled magnetosome chains, which on average are less extended toward subpolar-to-polar subcellular regions, coinciding with regions of predominant native CcfM localization (Fig. 1 *B*, *i*). Cells harboring appendages were found to often deviate from this general pattern, displaying elevated magnetosome numbers and multiple (≥3) and abnormally elongated chains (Fig. 3 *A*, *iv* and *v* and *SI Appendix*, Fig. S9*B*), further promoting an intriguing role of CcfM in magnetosome chain segregation.

Wild-type–like magnetosome chains and cell morphology were mostly restored upon chromosomal reinsertion of the *ccfM* wild-type allele into the Δ*ccfM* strain (Figs. 2 and 3 and *SI Appendix, Supplemental Results* and Fig. S9 *D* and *E*), suggesting that the observed phenotypes were due to loss of *ccfM*. Some complemented cells exhibited rather short or ectopic magnetosome chains, indicating that CcfM levels in the transcomplemented Δ*ccfM* strain were somewhat above native levels (Fig. 3 *A*, *xiii*, and *SI Appendix, Supplemental Results* and Fig. S9*D*). Remarkably, codeletion of *mamY* and *ccfM* caused a stronger reduction in cell curvature than in the Δ*ccfM* strain and severely affected magnetosome formation, pointing toward a synergistic genetic interaction between both mutations, and providing additional support for a functional relationship between CcfM, cell shape, and the magnetoskeleton (*SI Appendix, Supplemental Results* and Fig. S11).

Altogether, our data show that CcfM is not essential for primary magnetosome alignment and geodetic positioning of magnetosome chains per se, but promotes formation of long single chains of magnetosomes, which are more extended toward the poles. Furthermore, cell morphology defects of the Δ*ccfM* strain pointed toward an elusive function with respect to cell partitioning, segregation of magnetosome chains, and control of cell curvature.

CcfM Localizes in Filamentous Patterns in Closely and Distantly Related Bacteria. To further unveil what determines CcfM localization (e.g., cell geometry or other cytoskeletal proteins), we expressed CcfM fluorescent fusions in various closely and more distantly related heterologous hosts with different cell shapes (Fig. 4 and *SI Appendix*, Fig. S3 *E–J*). GFP-CcfM in rod-shaped *Escherichia coli* cells displayed circumferential patterns close to the membrane and perpendicular to the long axis of the cells as observed by 3D-SIM (Fig. 4 *A*, *i* and *SI Appendix*, Fig. S3 *E*, *i*) and conventional deconvolution microscopy (*SI Appendix*, Fig. S3*F*). Similar patterns were obtained with mTurq2-CcfM (*SI Appendix*, Fig. S3*G*) and mNG-CcfM fluorescent fusions (Fig. 4 *A*, *ii*, *SI Appendix*, Fig. S3*H*, and Movie S9), indicating that those are not a fluorophore-dependent artifact. These patterns are reminiscent of the localization of MreB in *E. coli* (42–44), suggesting a putative conserved interaction of CcfM with MreB. Remarkably, upon inducing formation of spheroplasts, circumferential CcfM-structures became disordered or even disappeared (Fig. 4 *A*, *iii* and *SI Appendix*, Fig. S3 *E*, *ii*), indicating that MreB-like localization of CcfM in *E. coli* relies on an intact cell wall. Similar localization patterns as in *M. gryphiswaldense*—including less pronounced longitudinal filamentous (Fig. 4 *B*, *i* and *SI Appendix*, Fig. S3 *I*, *i* and *ii*), and circumferential patterns (Fig. 4 *B*, *ii* and *SI Appendix*, Fig. S3 *I*, *iii* and *iv*)—were observed in a closely related nonmagnetotactic phototrophic Alphaproteobacterium, *Rhodospirillum rubrum*, which harbors an endogenous CcfM ortholog (Rru_A3216, 24.4% identity and 43.6% similarity to CcfM). *R. rubrum* has a helical morphology as *M. gryphiswaldense*, but is approximately twice as large in size (45). In the ovoid Alphaproteobacterium *Rhodobacter sphaeroides*, which lacks an endogenous CcfM ortholog, GFP-CcfM localized in clusters or foci at the membrane

(Fig. 4*C* and *SI Appendix*, Fig. S3*J*), reminiscent of the localization of MreB previously reported for *R. sphaeroides* (46). In *C. crescentus*, GFP-CcfM mostly localized to both cell poles, being more prominent at the stalked pole, and adopting an arc-like localization (Fig. 4*D*). This pattern was contrary to our initial expectation that CcfM might localize to the positively curved shorter inner face of the cell body [i.e., resembling crescentin (20)], and might be a hint that interaction with specific subcellular structures present at the stalked pole (47, 48) favored localization of CcfM in polar arc-shaped structures.

In summary, CcfM is capable to localize in filamentous patterns that are often reminiscent of MreB localization in the absence of *M. gryphiswaldense*-specific proteins in closely and distantly related bacteria.

CcfM Interacts with MamK and MamY via Distinct Domains and with the Cytoskeleton via MreB. Based on our observations, we speculated that CcfM might interact with the magnetoskeleton and other cytoskeletal proteins, in particular MreB. Protein interactions between CcfM and candidate proteins were identified by bacterial adenylate cyclase (CyaA) two-hybrid assay (BACTH) (49). BACTH revealed medium to strong interactions (based on the intensity of blue color) between CcfM and MamK (three of eight combinations) (Fig. 5 *A*, *i*), and between CcfM and MamY (six of eight combinations) (Fig. 5 *A*, *ii*). We also observed strong self-interactions of CcfM, MamK, and MamY [in agreement with Toro-Nahuelpan et al. (8)], a prerequisite required for homo-oligomerization and filament formation. Two-hybrid experiments employing truncated CcfM variants (Fig. 5 *A*, *iii*) revealed that CcfM interacts with MamY solely via its short cytoplasmic N terminus and the membrane anchor, whereas the interaction with MamK is predominantly mediated by the long C-terminal coiled-coil–rich tail. In contrast, transmembrane segments and the C-terminal tail of CcfM were both able to mediate self-interaction with full-length CcfM.

Protein interactions were further supported by colocalization microscopy in *M. gryphiswaldense* (Fig. 5*B*). By 3D-SIM we found that the fluorescence signals of GFP-CcfM and of a mCherry fluorescent fusion to MamK [which forms dynamic filaments originating from the cell poles (4)] partially overlapped, and long segments at the minor cell axis with both filamentous structures in close proximity (Fig. 5 *B*, *i* and *ii*). We also observed cells harboring a second MamK filament located at opposing regions of negative inner membrane curvature that was not associated with CcfM, and MamK filaments that were partially associated with CcfM at the minor cell axis, and partially dislocated toward the major cell axis (Fig. 5 *B*, *i–iii*). Partially dislocated MamK filaments were frequent upon prolonged overexpression of GFP-CcfM (Fig. 5 *B*, *iii*), when cells became elongated and highly curved, and continuous but also ring-shaped CcfM localization was present. In addition, under such conditions, in some cells MamK signals became dispersed (Fig. 5 *B*, *iv*). The mCherry-MamK localization observed after prolonged expression of GFP-CcfM agrees with the observations of mispositioned or disrupted magnetosome chains by TEM (Fig. 1*E* and *SI Appendix*, Fig. S9*A*). In cells coexpressing mCherry-MamY and GFP-CcfM we also found partial overlap and a close proximity of both filamentous structures at regions of positive inner cell curvature, CcfM being more prominent in polar and subpolar regions and MamY around midcell (Fig. 5*C*). A possible association of CcfM with the magnetoskeleton was further supported by the notion that CcfM was not only found in the cellular membrane, but also detected within purified magnetosome fractions by proteomic analysis (*SI Appendix*, Fig. S12*A*), and from the previous pull-down of CcfM as putative interaction partner of the magnetosome-associated protein MamA in the related *Magnetospirillum magneticum* (50) (*SI Appendix, Supplemental Results* and Fig. S12 *B* and *C*).

MICROBIOLOGY
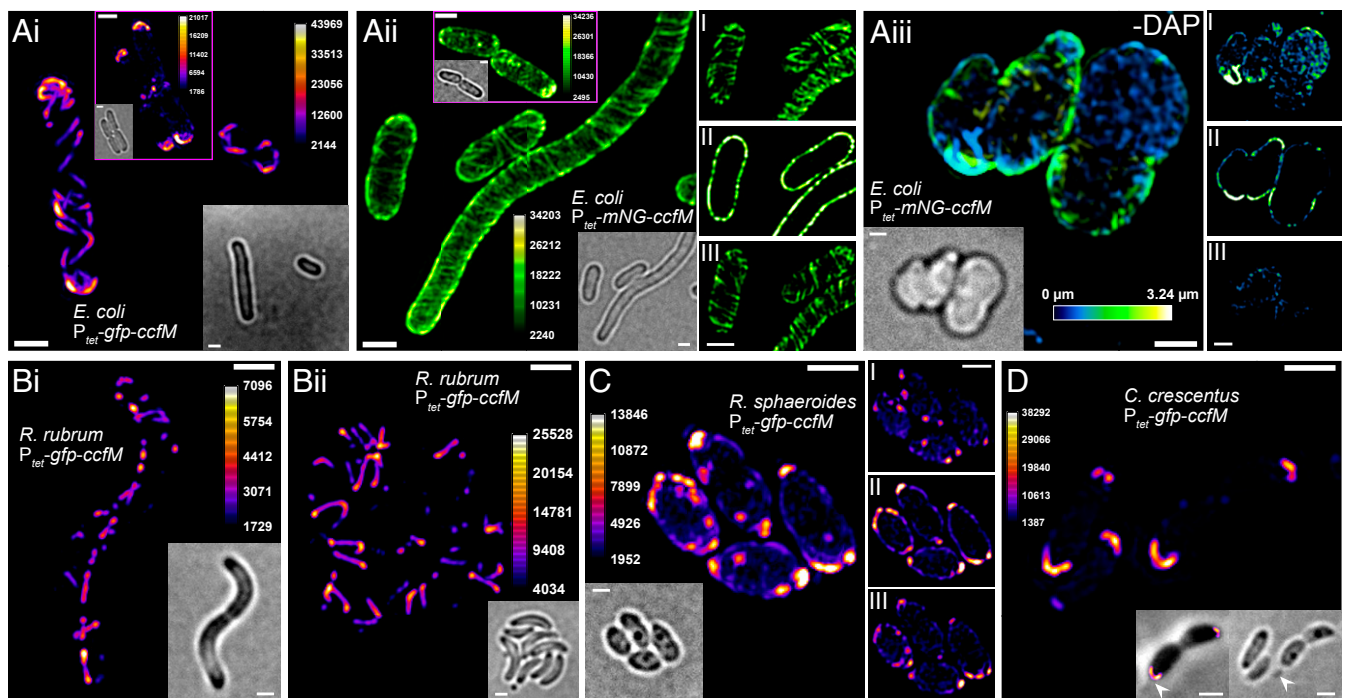
Fig. 4. Localization of CcfM in different bacteria. (*A*) Localization of GFP-CcfM (*i*) and mNeonGreen-CcfM (*ii*) in circumferential patterns in *E. coli* WM3064 (*i*, 21 h; *ii*, 24 h postinduction). After shorter induction times CcfM fluorescent fusions mostly localized to the membrane and polar caps (purple *Insets*; 2 h postinduction). Circumferential CcfM structures became disordered or disappeared when mNeonGreen-CcfM expressing 2,6-diaminopimelic acid (DAP)-auxotrophic *E. coli* WM3064 cells (as shown in *ii*) were incubated for 3 h in the absence of DAP (*iii*). (*B*) Localization of GFP-CcfM in *R. rubrum* in filamentous longitudinal (*i*) and circumferential (*i* and *ii*) patterns. The micrograph in *i* represents a cell of a culture grown under aerobic conditions in the dark (7 h postinduction), *ii* depicts cells of a culture grown in closed screw-cap tubes with illumination from a light bulb (without induction, leaky expression from P$_{tet}$). (*C*) In *R. sphaeroides*, GFP-CcfM localized to the membrane and to clusters more prominent in polar regions (7 h postinduction; culture grown under aerobic conditions in the dark). (*D*) In *C. crescentus*, GFP-CcfM localized at the polar caps in arc-like sheets, which were more prominent at the stalked pole (7 h postinduction; white arrowheads). All fluorescent fusions were expressed using the P$_{tet}$ promoter system. Main micrographs are 3D-SIM *z*-series maximum-intensity projections, except the depth-coded projection in *A*, *iii*. Calibration bars denote the intensity of fluorescence for the maximum-intensity projections and the focus distance into the sample for the depth-coded projection. Micrographs to the right in *A*, *ii*, *A*, *iii*, and *C* are selected *z*-slices depicting bottom, top (I, III), and central parts of the cells (II). Brightfield images are shown as *Inset*. In *D* an additional *Inset* (*Bottom Right*, *Left* image) depicts an overlay of the maximum-intensity projection and phase contrast. (Scale bars, 1 μm.)

BACTH also revealed a strong interaction (similar to the positive control) between CcfM and the *M. gryphiswaldense* MreB ortholog (MreB$_{Mgr}$, MSR1_17770) (Fig. 5*D*), which was only detected in one permutation, suggesting that interaction between CcfM and MreB$_{Mgr}$ is either sterically constrained, or limited due a competition of interacting sites, such as by means of high-affinity homo-oligomeric contacts. Treatment of GFP-CcfM expressing cells with the MreB-specific inhibitor A22 (16) indicated that MreB$_{Mgr}$ contributes to cell morphology control in *M. gryphiswaldense*, and is required to confer circumferential but not necessarily positive curvature dependent localization of CcfM (*SI Appendix, Supplemental Results* and Fig. S13). Attempts to replace *mreB$_{Mgr}$* with an allele coding for a MreB$_{Mgr}$ sandwich mCherry fusion (48) (to study MreB localization during CcfM overproduction) were unsuccessful, but when the fluorescent fusion was expressed from an inducible promoter it localized in a "MreB-like" manner in *M. gryphiswaldense* and *E. coli* (*SI Appendix, Supplemental Results* and Fig. S14).

CcfM Promotes Motility and Magnetotaxis in Structured Environments. Altered cell and magnetosome chain morphology of the Δ*ccfM* strain (Figs. 2 and 3) prompted us to investigate the influence of CcfM on motility and magnetotaxis (Fig. 6 and *SI Appendix, Supplemental Results* and Fig. S15). Both deletion (Fig. 6*A*) and overexpression (*SI Appendix,* Fig. S15) of *ccfM* caused formation of smaller aerotactic swim halos in motility soft agar (~80% and

~53% the diameter of wild-type halos, respectively), indicating that optimal cell morphology is important for motility in *M. gryphiswaldense*. Since a motility soft agar assay for magnetotaxis (9) (Fig. 6*B*) and analysis of the magnetic response (C_{mag}) (51) (Fig. 6*C*) revealed no or only slight differences in magnetic alignment between the wild-type and Δ*ccfM* strain, we performed motility tracking using a microscope with a 3D magnetic coil set-up (9) to study motility in defined magnetic fields without consideration of growth or cell shape-dependent light-scattering effects. These experiments indicated that the Δ*ccfM* strain has an impaired motility and magnetic alignment if the complexity of the surrounding environment is increased, as noted by the 8 to 11% decreased average swimming speeds and a lower population median alignment score (9) of the Δ*ccfM* strain in comparison to the wild-type in methylcellulose-containing medium (Fig. 6*D*). Thus, CcfM contributes to effective motility and magnetotaxis if maintained at wild-type levels.

Discussion

After the recent description of MamY in *M. gryphiswaldense* as a core constituent and topological landmark for geodetic magnetosome positioning (8), and the actin-like MamK required for magnetosome chain formation and segregation (2–5), we report an additional cytoskeletal determinant in *M. gryphiswaldense*, the curvature-inducing coiled-coil protein CcfM. Based on its localization and interactions, we propose CcfM as a cytolinker between the magnetoskeleton and intrinsic cytoskeleton in *M. gryphiswaldense*
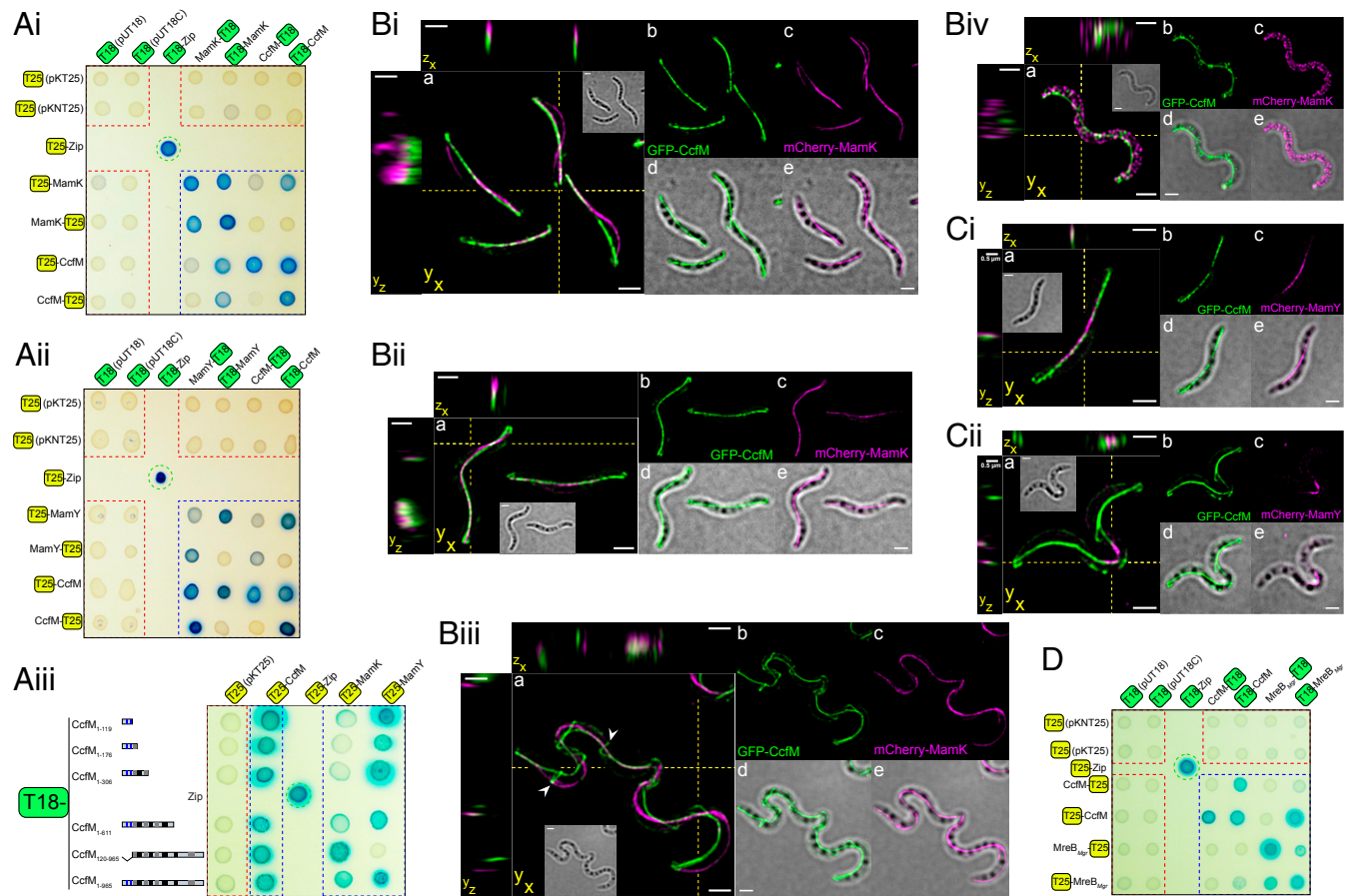
Fig. 5. CcfM interacts with MamK, MamY, and MreB$_{Mgr}$. (*A*) BACTH assay based on reconstitution of CyaA activity in an *E. coli cya⁻* strain. Fusion of interacting proteins to *Bordetella pertussis* CyaA catalytic domain complementary fragments T25 and T18 (which are inactive when physically separated) confers cAMP-dependent expression of catabolic genes, resulting in blue color formation and enhanced growth on X-Gal containing M63 maltose-mineral salts agar. Positive control (Leucine zipper) and negative controls (T18- or T25-fusions tested against the corresponding empty vector) are marked by green and red dashed lines, respectively. Tested interactions are marked by blue dashed lines. (*i*) BACTH analysis between CcfM and MamK and between (*ii*) CcfM and MamY. (*iii*) BACTH analysis of truncated CcfM variants against full-length T25-CcfM/MamK/MamY fusions. Numbers indicate amino acid positions. Putative transmembrane helices are marked in blue. Gray and black boxes represent putative coiled-coil motifs. Homo-oligomerization permutations of full-length CcfM (amino acids 1 to 965) were included on all plates for comparison. (*B*) The 3D-SIM colocalization microscopy of CcfM and MamK and (*C*) CcfM and MamY. GFP-CcfM was expressed from Tn5-P$_{tet}$ in the strains *mamK::mCherry-mamK* and *mamY::mCherry-mamY*. Micrographs were acquired 3 h (*B, i* and, *C, i*), 6 h (*B, ii*), and 24 h (*B, iii* and *iv*, and *C, ii*) postinduction. For each subfigure: (*a*) Color merge of *z*-stack maximum-intensity projections of both fluorescence channels (brightfield image shown as *Inset*). Yellow dashed lines and letters indicate orthogonal cross-sections shown to the top and left of the image. GFP-CcfM is colored in green; mCherry-MamK and -MamY are colored in magenta. White-colored regions indicate colocalization. Ring-shaped GFP-CcfM structures are indicated by white arrowheads. To correct for color shift, the microscope was calibrated with a bead sample and mismatch between channels was corrected during 3D-SIM image reconstruction. No significant cross-bleed of fluorescent fusions into the corresponding channel used to image the second fluorescent protein was detected. (*b* and *c*) Individual fluorescence channel images. Micrographs are maximum intensity projections. (*d* and *e*) Merge of individual fluorescence channels and brightfield. (All scale bars not indicated in the figure, 1 μm.) (*D*) BACTH analysis of CcfM and MreB$_{Mgr}$.

(Fig. 7). We suggest that CcfM integrates functions with respect to the control of cell shape with the proper formation and inheritance of magnetosome chains. This favors the formation of a coherent single chain that extends toward subpolar-to-polar subcellular regions, in agreement with the native localization of CcfM, thus maximizing the cellular magnetic dipole. Interactions between morphology-determining cytoskeletal proteins have been also suggested in other bacteria (52–54), implying that these are a common feature to maintain structural and functional integrity of the cytoskeleton.

CcfM Localization and Cell Curvature Promoting Functions. Based on its strong homo-oligomerization capability (Fig. 5*A* and *SI Appendix*, Fig. S8) and intrinsically disordered character, and supported by the observation of a putative CcfM-related structure underneath the inner membrane (Fig. 1*F*), we conclude that

CcfM forms a flexible membrane-attached scaffold, stabilized by interactions mediated by both the elongated coiled-coil–rich C terminus, and the N-terminal transmembrane-spanning segments (Fig. 7 and *SI Appendix, Supplemental Discussion*). Intrinsic positive membrane curvature-sensing properties of multimeric assemblies (55, 56) might confer preferential localization of CcfM at inwardly bending regions of the cell envelope. The localization experiments of our study (Figs. 1 and 4 and *SI Appendix*, Fig. S3) also suggest that CcfM adopts distinct localization patterns against its curvature preference, at the cell poles, at the major cell axis, or in circumferential patterns, depending on expression level and genetic background (i.e., architecture and geometry of the cell envelope, and availability of potential CcfM interactors) (*SI Appendix, Supplemental Discussion*). Multimeric CcfM assemblies might promote cell curvature directly—for example, by exerting a bending force onto the membrane (55, 56)—a hypothesis supported by the
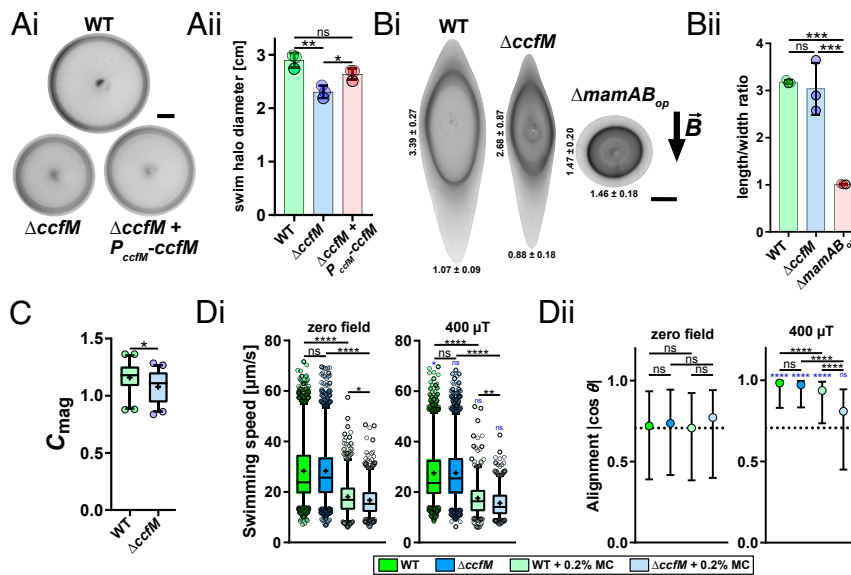
Fig. 6. CcfM promotes motility and magnetotaxis in structured environments. (*A, i*) Representative swim halos of the wild-type (WT), the Δ*ccfM* strain, and the transcomplemented Δ*ccfM* strain (Δ*ccfM* + Tn7-P*ccfM*-*ccfM*). Plates were incubated for 3 d at 28 °C under atmospheric conditions. (Scale bar, 0.5 cm.) (*ii*) Average swim halo diameters (±SDs). (*B, i*) Representative distorted swim halos formed after 2 d within a homogeneous 400-μT magnetic field (direction indicated by black arrow). For comparison, a nonmagnetic strain (Δ*mamAB*op) is shown. (Scale bar, 0.5 cm.) Average lengths and widths (±SDs) of the halos (in centimeters) are indicated. (*ii*) Average (±SDs) length-to-width ratios (vertical/horizontal diameter) of ellipsoid swim halos as a measure of magnetic alignment. Results in *A* and *B* are based on three individual experiments (performed in different weeks), each based on triplicate culture samples (considered here as subsamples). Statistical comparison of subsample averages (colored dots) was performed by one-way analysis of variance with Tukey's multiple-comparison posttest (*P < 0.05; **P < 0.01; ***P < 0.001; ns, not significant [P ≥ 0.05]). (*C*) Measurements of the magnetic response (*C*mag) based on individual cultures (wild-type, *n* = 45; Δ*ccfM*, *n* = 40) grown under microoxic conditions (2% headspace oxygen). In box plots: The bar indicates the median, the box the interquartile range, and the whiskers the 5th and 95th percentiles. Dots represent values below and above the 5th and 95th percentiles. The mean is shown as "+." Statistical analysis was performed by Mann–Whitney *U* test (*P < 0.05). (*D, i*) Swimming speeds and (*ii*) magnetic alignment determined by live-cell motility tracking in flask standard medium (FSM) and in FSM + 0.2% methylcellulose (MC) within a zero field (canceled geomagnetic field) and in a homogeneous 400-μT magnetic field. *θ* denotes the angle between the velocity vector and the axis of the magnetic field for a swimming track. A population median of the absolute cos *θ* of "1" indicates that cells swim aligned with the applied magnetic field, a value of "0" indicates alignment with the axis in the focal plane perpendicular to the magnetic field, and a value of ~0.7 (vertical dashed line) indicates an unbiased directional movement. Data were pooled from five experiments (performed on different days), corresponding to total track numbers of *n* = 1,669 (wild-type), 1,519 (Δ*ccfM*), 605 (wild-type + 0.2% MC), and 602 (Δ*ccfM* + 0.2% MC) within the zero field and 1,485 (wild-type), 1,559 (Δ*ccfM*), 381 (wild-type + 0.2% MC), and 521 (Δ*ccfM* + 0.2% MC) within the 400-μT magnetic field. Box plots in *D, i* are as described above. In *D, ii* dots depict the median and error bars the interquartile range. *P* values were determined by the Kruskal–Wallis test with Dunn's multiple comparison posttest; *P < 0.05; **P < 0.01; ****P < 0.0001; ns, not significant (P ≥ 0.05). Statistical comparison for the 400-μT magnetic field was additionally performed against the corresponding zero field condition (indicated by blue letters).

presence of putative apolipoprotein-like motifs within the C-terminal coiled-coil-rich tail of CcfM (*SI Appendix*, Fig. S1*B* and Table S1). Such motifs were discussed to mediate membrane interactions within eukaryotes (33–35, 57) and prokaryotes (36), by changing from a closed α-helix bundle to an open conformation (*SI Appendix, Supplemental Discussion* and Fig. S1*C*).

We further propose that CcfM may affect cell curvature by modulating MreB's localization and/or dynamics, to spatially control cell wall synthesis (Fig. 7 and *SI Appendix, Supplemental Discussion*). Encouraged by the conserved interaction of CcfM with MreB (Figs. 4 and 5*D*), and co-occurrence of both proteins also in nonmagnetotactic Alphaproteobacteria (*SI Appendix*, Fig. S2), we hypothesize that CcfM and MreB might be part of a common cell morphology-related module in Alphaproteobacteria with helical shape. How the interplay between CcfM and MreB affects cell curvature, and thus helicity, needs to be determined in future studies interrogating cell wall assembly and dynamics in a 3D fashion (11, 27). The finding that deletion of *ccfM* resulted only in a moderately decreased, but not complete loss of curved cell shape (Fig. 2), as well as the complexity of underlying determinants for helical cell shape in non-MTB (14), suggest that additional cytoskeletal determinants must be involved in regulating *M. gryphiswaldense* cell morphology, such as the uncharacterized bactofilin MSR1_22350, which might be functionally connected to CcfM (*SI Appendix, Supplemental Discussion*).

Interplay between CcfM and the Magnetoskeleton. We propose that CcfM extends the MamY scaffold toward the poles to form an entire cell-spanning geodetic scaffold (Fig. 7 and *SI Appendix, Supplemental Discussion*), stabilized by a direct interaction between both proteins that is mediated via the CcfM membrane-spanning segments (Fig. 5 *A* and *C*). A possible functional association of CcfM and MamY as a geodetic scaffold in MTB with curved shape is strengthened by the co-occurrence of MamK, MamY, and CcfM in spirilla-shaped or vibrioid MTB, but absence of both CcfM and MamY in spherical and rod-shaped MTB (*SI Appendix*, Fig. S2), as well as by the synergistic effects observed upon codeletion of both genes (*SI Appendix*, Fig. S11). In comparison to MamY, which was suggested to directly function as topological landmark that mediates geodetic magnetosome chain localization (8), CcfM may act as a membrane-attached scaffold to guide treadmilling MamK filaments originating at the cell poles (4) to the geodetic axis of the cell, by direct interaction of the CcfM coiled-coil-rich tail part with MamK (Fig. 5 *A, iii*). MamK filaments that can bend and twist (8) may tend to locate to the major cell axis when CcfM is absent, or when the stochiometric ratio between CcfM, MamY, and MamK is changed (e.g., Fig. 5 *B, iii*), supported by the finding of misplaced or entirely scattered magnetosome chains upon artificial CcfM overproduction (Fig. 1*E* and *SI Appendix, Supplemental Discussion* and Fig. S9*A*). Hence, CcfM might promote MamK-dynamics dependent repositioning of magnetosomes
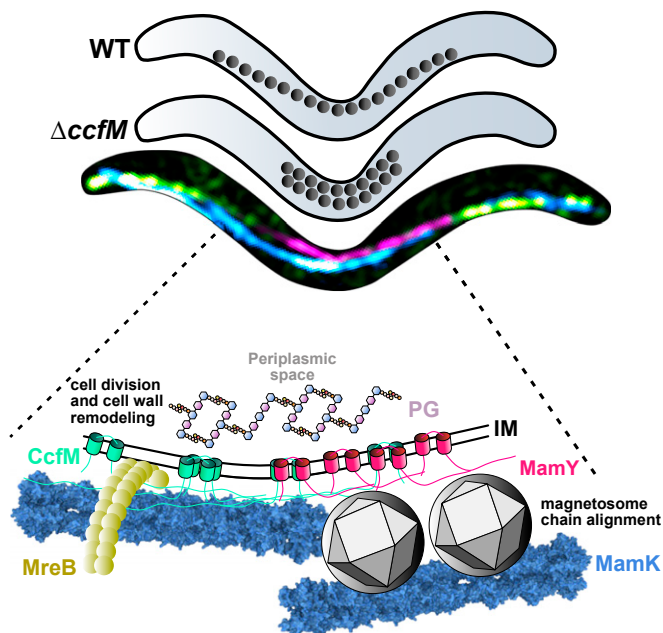
Fig. 7. Model of CcfM molecular interactions with the cytoskeleton and magnetoskeleton. Suggested interactions identified (or confirmed) in this study are between CcfM and MamY (mediated via CcfM transmembrane helices), CcfM and MamK (mediated via CcfM coiled-coil motifs), CcfM and MreB, and homo-oligomerization interactions of CcfM, MamK, MamY, and MreB. Magnetosomes are concatenated into chains by MamJ-mediated attachment to MamK (for simplicity only MamK is shown). Magnetosome chains are aligned along regions of positive inner-cell curvature via MamY. Based on its native localization pattern, which is characterized by a predominant assembly at subpolar-to-polar regions of the inner positively curved membrane, CcfM might serve as supportive structure to confer geodetic localization of MamK. CcfM might extend the MamY membrane tether and magnetoskeleton toward the poles, favoring assembly of shorter, doubled chains when CcfM is absent (as indicated in the schematic drawing on top). CcfM also has a role related to cell division and morphology. CcfM might reinforce curved cell shape by exerting a bending force onto the inner membrane, and/or by interaction with MreB (e.g., by modulating MreB's localization and dynamics), which may spatially affect insertion of new peptidoglycan building units. Note, possible direct interactions between MamK, MamY, and MreB so far have not been experimentally addressed. Molecular dimensions are not drawn to scale. For simplicity only the α-helical transmembrane segments of CcfM are indicated as cylinders. IM, inner cellular membrane; PG, peptidoglycan. The fluorescence micrograph was created from two separate cells with similar shape expressing GFP-CcfM (green) and mCherry-MamY (magenta) or mCherry-MamK (cyan), respectively, which were stitched together to illustrate the localization of all three proteins.

from the new cell poles to midcell in recently divided cells, and magnetosome attachment to the MamY scaffold. Loss of a functional association of CcfM with the magnetoskeleton in the Δ*ccfM* strain is supported by the higher propensity of cells forming shorter, doubled magnetosome chains (Fig. 3 *C* and *D*), appearance of scattered magnetite particles toward the parts of the magnetosome chain approaching subpolar inwardly bend regions of the cell envelope (Fig. 3*A*), and magnetosomes that lost attachment to MamK within tubular extensions of the cell envelope connecting future daughter cells (Fig. 3*B*). Future studies should aim to analyze MamK dynamics with relation to CcfM.

Role of CcfM for Motility and Magnetotaxis. As indicated by the efficiency of swim halo formation in motility soft agar and tracking microscopy (Fig. 6), CcfM had a positive effect on motility and magnetotaxis in structured environments when present at native

levels. The increased cell length and reduced curvature (in 2D) of the Δ*ccfM* strain (Fig. 2) point toward an altered helical pitch of the cell body, which may affect flagella-driven propulsion in structured media, likely causing the observed size decrease of swim halos and reduced swimming speeds in methylcellulose-containing medium (Fig. 6 *A*, *B*, and *D*, *i*). A 7 to 21% reduction in median swimming speeds of isogenic *H. pylori* mutants exhibiting straight-rod morphology in broth and different gel-like media suggested that helical cell morphology enhances motility and swimming speed (12). Similarly, noncurved *V. cholerae* cells lacking the periplasmic curvature determinant CrvA were impaired to migrate in soft agar, in particular with increasing agar concentration (11). The impaired magnetic alignment of the Δ*ccfM* strain in methylcellulose-containing medium (Fig. 6 *D*, *ii*) suggests that CcfM affects cell and magnetosome chain morphology to warrant optimal motility and magnetic navigation in structured environments, resembling conditions that are more comparable to natural environments. In particular, a longer cell-spanning single magnetosome chain likely causes a higher cellular magnetic dipole moment, providing a more efficient and stable magnetic alignment of the helical cell body when the extracellular environment causes cells to frequently deviate from the axis of the magnetic field.

In conclusion, we assigned first functions to a cytoskeletal constituent in *M. gryphiswaldense* required for optimal magnetotaxis by integration of cell shape-dependent effects with the regulation of magnetosome chain formation. Based on our observations of rather subtle effects under artificial laboratory conditions, we predict that CcfM possesses a much more important role in complex environmental habitats of MTB, such as the highly structured muddy sediments of their native aquatic habitats, resulting in a substantial increase in fitness under natural conditions. Our results further suggest that CcfM levels need to be tightly regulated to warrant contributive effects on magnetosome chain positioning, cell shape, and hence motility. It will therefore be interesting to analyze whether CcfM expression is regulated in response to extracellular conditions, to modulate cell curvature and magnetosome chain morphology for most efficient magnetotaxis within the respective environment. Further efforts are necessary to analyze how CcfM functions together with MreB to modulate cell shape, or with MamK and MamY to control the formation of a coherent cell-spanning magnetosome chain, and to reveal unidentified molecular interactions between the cytoskeleton and magnetoskeleton. Finally, a deeper understanding of cell shape control in MTB is also of high relevance for future technical and biomedical applications, for example, for the construction of magnetically steered bio-inspired swimming robots with improved properties in viscous environments (14, 58).

Materials and Methods

Bacterial Strains, Plasmids, and Culture Conditions. Plasmid and strains (listed in *SI Appendix*, Table S2) were constructed using standard molecular biology methods (oligonucleotides are listed in *SI Appendix*, Table S3) described in detail in *SI Appendix*. Cells were grown as described previously (38, 59) and in *SI Appendix*.

Fluorescence Microscopy. Sample preparation employing "MSR agarose pads," imaging of fluorescent protein fusions, and image processing and analysis were conducted as specified previously (4, 38) and in *SI Appendix*.

TEM and CET. TEM and CET were performed as described previously (4). Detailed information is also provided in the *SI Appendix*.

Two-Hybrid Assay. To conduct protein interaction studies, the CyaA-based two-hybrid assay was used (49), which is based on the reconstitution of CyaA activity in the *cyaA*-deficient *E. coli* BTH101 strain. Construction of CyaA fragment fusion proteins and identification of protein interactions was performed as described in *SI Appendix*.

Motility Assays. Motility soft agar assays were performed employing 0.2% agar (wt/vol) plates and cultures adjusted in their cell density to ensure reproducibility as reported previously (9) and in *SI Appendix*. Single-cell tracking was performed in dark-field illumination using a custom microscopic setup based on a FN1 Eclipse upright microscope (Nikon) equipped with an S Plan Fluor 20× differential inference contrast (DIC) N1 objective (NA0.5), a dark-field condenser (NA0.95), a pco.edge 4.2 sCMOS camera (PCO), and custom-made triaxial pairs of magnetic coils (9). Measurements were performed on early log-phase cells grown in flask standard liquid medium (59) under microoxic conditions (2% headspace oxygen, 28 °C) using sample preparation, video recording, and cell tracking settings described previously (9).

Statistical Analysis. Statistical analysis was performed in Prism 7.04 (GraphPad) as described in the respective legend to each figure. Datasets were tested for normality using the D'Agostino and Pearson, Shapiro–Wilk, and Kolmogorov–Smirnov tests.

Data Availability. All study data are included in the article and supporting information.

1. R. Uebe, D. Schüler, Magnetosome biogenesis in magnetotactic bacteria. *Nat. Rev. Microbiol.* **14**, 621–637 (2016).
2. A. Komeili, Z. Li, D. K. Newman, G. J. Jensen, Magnetosomes are cell membrane invaginations organized by the actin-like protein MamK. *Science* **311**, 242–245 (2006).
3. E. Katzmann, A. Scheffel, M. Gruska, J. M. Plitzko, D. Schüler, Loss of the actin-like protein MamK has pleiotropic effects on magnetosome formation and chain assembly in Magnetospirillum gryphiswaldense. *Mol. Microbiol.* **77**, 208–224 (2010).
4. M. Toro-Nahuelpan et al., Segregation of prokaryotic magnetosomes organelles is driven by treadmilling of a dynamic actin-like MamK filament. *BMC Biol.* **14**, 88 (2016).
5. E. Katzmann et al., Magnetosome chains are recruited to cellular division sites and split by asymmetric septation. *Mol. Microbiol.* **82**, 1316–1329 (2011).
6. A. Scheffel et al., An acidic protein aligns magnetosomes along a filamentous structure in magnetotactic bacteria. *Nature* **440**, 110–114 (2006).
7. O. Draper et al., MamK, a bacterial actin, forms dynamic filaments in vivo that are regulated by the acidic proteins MamJ and LimJ. *Mol. Microbiol.* **82**, 342–354 (2011).
8. M. Toro-Nahuelpan et al., MamY is a membrane-bound protein that aligns magnetosomes and the motility axis of helical magnetotactic bacteria. *Nat. Microbiol.* **4**, 1978–1989 (2019).
9. D. Pfeiffer, D. Schüler, Quantifying the benefit of a dedicated "magnetoskeleton" in bacterial magnetotaxis by live-cell motility tracking and soft agar swimming assay. *Appl. Environ. Microbiol.* **86**, e01976–e19 (2020).
10. S. Rismani Yazi, R. Nosrati, C. A. Stevens, D. Vogel, C. Escobedo, Migration of magnetotactic bacteria in porous media. *Biomicrofluidics* **12**, 011101 (2018).
11. T. M. Bartlett et al., A periplasmic polymer curves Vibrio cholerae and promotes pathogenesis. *Cell* **168**, 172–185.e15 (2017).
12. L. E. Martínez et al., Helicobacter pylori strains vary cell shape and flagellum number to maintain robust motility in viscous environments. *Mol. Microbiol.* **99**, 88–110 (2016).
13. S. Schätzle, M. Specht, B. Waidner, Coiled coil rich proteins (Ccrp) influence molecular pathogenicity of Helicobacter pylori. *PLoS One* **10**, e0121463 (2015).
14. J. A. Taylor, S. R. Sichel, N. R. Salama, Bent bacteria: A comparison of cell shape mechanisms in proteobacteria. *Annu. Rev. Microbiol.* **73**, 457–480 (2019).
15. H. C. Berg, L. Turner, Movement of microorganisms in viscous environments. *Nature* **278**, 349–351 (1979).
16. H. Shi, B. P. Bratton, Z. Gitai, K. C. Huang, How to build a bacterial cell: MreB as the foreman of E. coli construction. *Cell* **172**, 1294–1305 (2018).
17. J. Wagstaff, J. Löwe, Prokaryotic cytoskeletons: Protein filaments organizing small cells. *Nat. Rev. Microbiol.* **16**, 187–201 (2018).
18. S. Hussain et al., MreB filaments align along greatest principal membrane curvature to orient cell wall synthesis. *eLife* **7**, e32471 (2018).
19. L. Lin, M. Thanbichler, Nucleotide-independent cytoskeletal scaffolds in bacteria. *Cytoskeleton (Hoboken)* **70**, 409–423 (2013).
20. N. Ausmees, J. R. Kuhn, C. Jacobs-Wagner, The bacterial cytoskeleton: An intermediate filament-like function in cell shape. *Cell* **115**, 705–713 (2003).
21. M. T. Cabeen et al., Bacterial cell curvature through mechanical control of cell growth. *EMBO J.* **28**, 1208–1219 (2009).
22. G. Charbon, M. T. Cabeen, C. Jacobs-Wagner, Bacterial intermediate filaments: In vivo assembly, organization, and dynamics of crescentin. *Genes Dev.* **23**, 1131–1144 (2009).
23. B. Waidner et al., A novel system of cytoskeletal elements in the human pathogen Helicobacter pylori. *PLoS Pathog.* **5**, e1000669 (2009).
24. L. K. Sycuro et al., Peptidoglycan crosslinking relaxation promotes Helicobacter pylori's helical shape and stomach colonization. *Cell* **141**, 822–833 (2010).
25. M. Specht, S. Schätzle, P. L. Graumann, B. Waidner, Helicobacter pylori possesses four coiled-coil-rich proteins that form extended filamentous structures and control cell shape and motility. *J. Bacteriol.* **193**, 4523–4530 (2011).
26. K. M. Blair et al., The Helicobacter pylori cell shape promoting protein Csd5 interacts with the cell wall, MurF, and the bacterial cytoskeleton. *Mol. Microbiol.* **110**, 114–127 (2018).
27. J. A. Taylor et al., Distinct cytoskeletal proteins define zones of enhanced cell wall synthesis in Helicobacter pylori. *eLife* **9**, e52482 (2020).
28. K. M. Jackson, C. Schwartz, J. Wachter, P. A. Rosa, P. E. Stewart, A widely conserved bacterial cytoskeletal component influences unique helical shape and motility of the spirochete Leptospira biflexa. *Mol. Microbiol.* **108**, 77–89 (2018).
29. L. Slamti, M. A. de Pedro, E. Guichet, M. Picardeau, Deciphering morphological determinants of the helix-shaped Leptospira. *J. Bacteriol.* **193**, 6266–6275 (2011).
30. A. K. Fenton, L. Hobley, C. Butan, S. Subramaniam, R. E. Sockett, A coiled-coil-repeat protein 'Ccrp' in Bdellovibrio bacteriovorus prevents cellular indentation, but is not essential for vibroid cell morphology. *FEMS Microbiol. Lett.* **313**, 89–95 (2010).
31. H. Lam, W. B. Schofield, C. Jacobs-Wagner, A landmark protein essential for establishing and perpetuating the polarity of a bacterial cell. *Cell* **124**, 1011–1023 (2006).
32. E. Huitema, S. Pritchard, D. Matteson, S. K. Radhakrishnan, P. H. Viollier, Bacterial birth scar proteins mark future flagellum assembly site. *Cell* **124**, 1025–1037 (2006).
33. J. Wang, B. D. Sykes, R. O. Ryan, Structural basis for the conformational adaptability of apolipophorin III, a helix-bundle exchangeable apolipoprotein. *Proc. Natl. Acad. Sci. U.S.A.* **99**, 1188–1193 (2002).
34. J. Wang, S. M. Gagné, B. D. Sykes, R. O. Ryan, Insight into lipid surface recognition and reversible conformational adaptations of an exchangeable apolipoprotein by multidimensional heteronuclear NMR techniques. *J. Biol. Chem.* **272**, 17912–17920 (1997).
35. M. Mirheydari, E. K. Mann, E. E. Kooijman, Interaction of a model apolipoprotein, apoLp-III, with an oil-phospholipid interface. *Biochim. Biophys. Acta Biomembr.* **1860**, 396–406 (2018).
36. J. R. Zupan, P. Grangeon, J. S. Robalino-Espinosa, N. Garnica, P. Zambryski, GROWTH POLE RING protein forms a 200-nm-diameter ring structure essential for polar growth and rod shape in Agrobacterium tumefaciens. *Proc. Natl. Acad. Sci. U.S.A.* **116**, 10962–10967 (2019).
37. E. Krol et al., Tol-pal system and Rgs proteins interact to promote unipolar growth and cell division in Sinorhizobium meliloti. *MBio* **11**, e00306–e00320 (2020).
38. D. Pfeiffer, M. Toro-Nahuelpan, M. Bramkamp, J. M. Plitzko, D. Schüler, The polar organizing protein PopZ is fundamental for proper cell division and segregation of cellular content in Magnetospirillum gryphiswaldense. *MBio* **10**, e02716–e02718 (2019).
39. N. C. Shaner et al., A bright monomeric green fluorescent protein derived from Branchiostoma lanceolatum. *Nat. Methods* **10**, 407–409 (2013).
40. J. Goedhart et al., Structure-guided evolution of cyan fluorescent proteins towards a quantum yield of 93%. *Nat. Commun.* **3**, 751 (2012).
41. K. Heinrich, D. J. Leslie, M. Morlock, K. Bertilsson, K. Jonas, Molecular basis and ecological relevance of Caulobacter cell filamentation in freshwater habitats. *MBio* **10**, e01557–e19 (2019).
42. T. Kruse, J. Møller-Jensen, A. Løbner-Olesen, K. Gerdes, Dysfunctional MreB inhibits chromosome segregation in Escherichia coli. *EMBO J.* **22**, 5283–5292 (2003).
43. Y.-L. Shih, T. Le, L. Rothfield, Division site selection in Escherichia coli involves dynamic redistribution of Min proteins within coiled structures that extend between the two cell poles. *Proc. Natl. Acad. Sci. U.S.A.* **100**, 7865–7870 (2003).
44. M. T. Swulius, G. J. Jensen, The helical MreB cytoskeleton in Escherichia coli MC1000/pLE7 is an artifact of the N-Terminal yellow fluorescent protein tag. *J. Bacteriol.* **194**, 6382–6386 (2012).
45. I. Kolinko et al., Biosynthesis of magnetic nanostructures in a foreign organism by transfer of bacterial magnetosome gene clusters. *Nat. Nanotechnol.* **9**, 193–197 (2014).
46. P. M. Slovak, G. H. Wadhams, J. P. Armitage, Localization of MreB in Rhodobacter sphaeroides under conditions causing changes in cell shape and membrane structure. *J. Bacteriol.* **187**, 54–64 (2005).
47. J. Kühn et al., Bactofilins, a ubiquitous class of cytoskeletal proteins mediating polar localization of a cell wall synthase in Caulobacter crescentus. *EMBO J.* **29**, 327–339 (2010).
48. M. Billini, J. Biboy, J. Kühn, W. Vollmer, M. Thanbichler, A specialized MreB-dependent cell wall biosynthetic complex mediates the formation of stalk-specific peptidoglycan in Caulobacter crescentus. *PLoS Genet.* **15**, e1007897 (2019).

49. G. Karimova, A. Ullmann, D. Ladant, A bacterial two-hybrid system that exploits a cAMP signaling cascade in Escherichia coli. *Methods Enzymol.* **328**, 59–73 (2000).
50. H. V. Nguyen *et al.*, A protein-protein interaction in magnetosomes: TPR protein MamA interacts with an Mms6 protein. *Biochem. Biophys. Rep.* **7**, 39–44 (2016).
51. D. Schüler, R. Uhl, E. Bäuerlein, A simple light scattering method to assay magnetism in Magnetospirillum gryphiswaldense. *FEMS Microbiol. Lett.* **132**, 139–145 (1995).
52. N. A. Holmes *et al.*, Coiled-coil protein Scy is a key component of a multiprotein assembly controlling polarized growth in Streptomyces. *Proc. Natl. Acad. Sci. U.S.A.* **110**, E397–E406 (2013).
53. K. Sundararajan, E. D. Goley, Cytoskeletal proteins in Caulobacter crescentus: Spatial orchestrators of cell cycle progression, development, and cell shape. *Subcell. Biochem.* **84**, 103–137 (2017).
54. B. L. Springstein *et al.*, Identification and characterization of novel filament-forming proteins in cyanobacteria. *Sci. Rep.* **10**, 1894 (2020).
55. H. T. McMahon, E. Boucrot, Membrane curvature at a glance. *J. Cell Sci.* **128**, 1065–1070 (2015).
56. I. K. Jarsch, F. Daste, J. L. Gallop, Membrane curvature in cell biology: An integration of molecular mechanisms. *J. Cell Biol.* **214**, 375–387 (2016).
57. J. Varkey *et al.*, Membrane curvature induction and tubulation are common features of synucleins and apolipoproteins. *J. Biol. Chem.* **285**, 32486–32493 (2010).
58. K. E. Peyer, L. Zhang, B. J. Nelson, Bio-inspired magnetic swimming microrobots for biomedical applications. *Nanoscale* **5**, 1259–1272 (2013).
59. U. Heyen, D. Schüler, Growth and magnetosome formation by microaerophilic Magnetospirillum strains in an oxygen-controlled fermentor. *Appl. Microbiol. Biotechnol.* **61**, 536–544 (2003).

MICROBIOLOGY